Author Manuscript

Regional maps of rib cortical bone thickness and cross-sectional geometry

Sven A Holcombe[a,*], Yun-Seok Kang[c], Brian A Derstine[a], Stewart C Wang[a,b], Amanda M Agnew[c]

[a]*Morphomics Analysis Group, University of Michigan, Ann Arbor, MI, USA*
[b]*Department of Surgery, University of Michigan, Ann Arbor, MI, USA*
[c]*Injury Biomechanics Research Center, The Ohio State University, Columbus, OH, USA*

Abstract

Here we present detailed regional bone thickness and cross-sectional measurements from full adult ribs using high resolution CT scans processed with a cortical bone mapping technique. Sixth ribs from 33 subjects ranging from 24 to 99 years of age were used to produce average cortical bone thickness maps and to provide average±1SD corridors for expected cross-section properties (cross-sectional areas and inertial moments) as a function of rib length.

Results obtained from CT data were validated at specific rib locations using direct measurements from cut sections. Individual thickness measurements from CT had accuracy (mean error) and precision (SD error) of -0.013 ± 0.167 mm (R^2 coefficient of determination of 0.84). CT-based measurement errors for rib cross-sectional geometry were $-0.1 \pm 13.1\%$ (cortical bone cross-sectional area) and $4.7 \pm 1.8\%$ (total cross-sectional area).

Rib cortical bone thickness maps show the expected regional variation across a typical rib's surface. The local mid-rib maxima in cortical thickness

---

[*]Corresponding author
Email address: `svenho@umich.edu` (Sven A Holcombe)

along the pleural rib aspect ranged from 0.9 mm to 2.6 mm across the study population with an average map maximum of 1.4 mm. Along the cutaneous aspect, rib cortical bone thickness ranged from 0.7 mm to 1.9 mm with average map thickness of 0.9 mm. Average cross-sectional properties show a steady reduction in total cortical bone area from 10 % along the rib's length through to the sternal end, whereas overall cross-sectional area remains relatively constant along the majority of the rib's length before climbing steeply towards the sternal end. On average, male ribs contained more cortical bone within a given cross-section than was seen for female ribs. Importantly, however, this difference was driven by male ribs having larger overall cross-sectional areas, rather than by sex differences in the bone thickness observed at specific local cortex sites.

The cortical bone thickness results here can be used directly to improve the accuracy of current human body and rib models. Furthermore, the measurement corridors obtained from adult subjects across a wide age range can be used to validate future measurements from more widely available image sources such as clinical CT where gold standard reference measures (e.g., like direct measurements obtained from cut sections) are otherwise unobtainable.

Keywords: Cortical bone, Rib, Computed Tomography, Cortical thickness, Cross-sectional geometry, Computational models

---

1. Introduction

2   Ribs provide crucial protection for the thoracic viscera, but are often fractured in a variety of scenarios (Wuermser et al., 2011). In motor vehicle

4   crashes (MVCs) specifically, rib fractures continue to be prevalent despite

2

advances to safety systems and vehicles. Furthermore, the presence of rib

6 fractures increases mortality and morbidity rates in vulnerable populations (e.g., elderly) (Stawicki et al., 2004; Sirmali et al., 2003). Recent research has

8 highlighted the need for in-depth exploration of rib geometry to better understand whole thoracic response to loading (Murach et al., 2018), and therefore

10 develop injury mitigation techniques. Broadly, this can be accomplished using computational human body models (HBMs), an important modern tool

12 for injury assessment.

These models rely on accurate input for their prediction of a rib's response

14 to loading. Global and cross-sectional geometry have been identified as important predictors of this response in ribs (Stein, 1976; Agnew et al., 2013;

16 Murach et al., 2017; Agnew et al., 2018; Holcombe et al., 2016). Rib cortical bone thickness spans approximately 0.1 mm to 2.4 mm (Choi & Kwak,

18 2011; Mohr et al., 2007; Agnew et al., 2018) and is commonly represented in finite element (FE) computational models using shell elements surrounding

20 a solid trabecular core. Li et al. (2010) found that models which incorporate variable thickness into their cortical bone definitions can better predict

22 a rib's structural response. However, the precise distribution of thicknesses along and around rib bones is not well understood. Current sources report

24 thickness values only in aggregation across particular zones around the rib's circumference or along its length (Agnew et al., 2018; Mohr et al., 2007;

26 Mayeur et al., 2010). In most current models the rib global geometry is drawn from a single individual, and cortical bone thickness values are drawn

28 from these limited or simplified literature sources (Gayzik et al., 2011; Choi et al., 2009; Kemper et al., 2007). Furthermore, there is now evidence that

3

₃₀ cross-sectional bone area and bone distribution may contribute more than only cortical thickness in predicting rib structural properties (Agnew et al., ₃₂ 2018), highlighting the need to quantify all rib cross-sectional geometry more thoroughly across the population. Despite the current knowledge that pre- ₃₄ cise rib cross-geometry is crucial for predicting rib fracture properties, the incorporation of such geometry at the level of detail necessary to reflect true ₃₆ human variation has not been fully realized in current HBMs. When rib modifications are made to HBMs to simulate population-based differences, a ₃₈ greater emphasis is generally placed on altering material properties and gross thoracic geometry than cross-sectional rib geometry to achieve the desired ₄₀ structural results (Ito et al., 2009; Schoell et al., 2015).

The Cortical Bone Mapping (CBM) methodology allows for accurate mea- ₄₂ surements of these important geometric factors from CT imaging (Holcombe et al., 2018; Treece & Gee, 2015; Treece et al., 2010). CBM has been pre- ₄₄ viously applied to ribs for tracking bone thickness reductions after cancer therapy (Okoukoni et al., 2016), but it has not yet been used to report rib ₄₆ cortical bone thickness distributions from individuals or across populations.

In this study we apply the CBM method to high resolution CT scans of full ₄₈ ribs. We assess the accuracy of this method against cross-sectional histology images taken at key locations along each rib, and develop full cortical bone ₅₀ thickness maps along and around individual ribs. We spatially register these maps from multiple individuals to present a detailed average thickness map ₅₂ that is representative of an American adult population. The methodology presented here can be used to build individualized rib models, while the ₅₄ aggregated maps can be applied to enhance general population models.

4

2. Materials and methods

⁵⁶   This study utilizes histology images extracted from, and CT image data covering, 33 complete sixth-level ribs ethically obtained from anatomical ⁵⁸ donors in Ohio, USA (16 male, 17 female) with no existing trauma or gross pathological condition affecting the ribs. Subject ages ranged from 24 to ⁶⁰ 99 years (average±SD 65 ± 21) with distributions shown by sex in Figure 1. Male subjects (70 ± 18 years) were on average older than female ⁶² subjects (60 ± 22 years), however this difference was not statistically significant ($p = 0.15$).

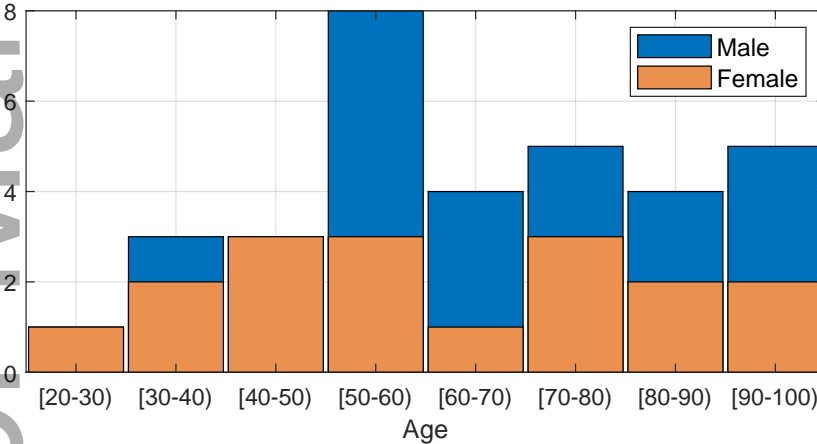Figure 1: Stacked subject age counts by sex and decade of life.

⁶⁴   Complete ribs were excised from subjects soon after death, and subsequently CT scans of each rib wrapped in saline-soaked gauze were taken ⁶⁶ using a Phillips Vereos digital PET/CT with 64 slice Ingenuity technology at an axial resolution of $0.15\,\mathrm{mm/pixel}$ with slice spacing of $0.67\,\mathrm{mm/pixel}$ ⁶⁸ (i.e., $0.15 \times 0.15 \times 0.67$ mm voxels). Ribs were oriented with their end-to-end axis aligned vertically in the scan such that mid-rib regions were approxi-

5

mately co-planar with the scan's axial plane. After experimental bending
tests, cross-sections perpendicular to the long axis of the rib were taken
immediately adjacent to each fracture site (39 total sites at either one or
two fracture sites per rib) while ensuring no disruption to the bone cortex.
Approximate fracture site locations—measured manually using string—were
noted as a percentage of rib curvilinear length. Slides were then prepared
according to undecalcified hard tissue histology standards (see Agnew et al.
(2018)). High-resolution microscopy (Olympus BX61VS) allowed for direct
image capture (*i.e.,* no reconstruction) of the entire rib section at 100x total
magnification and a resolution of 0.69 microns/pixel.

2.1. Histology image processing

Periosteal and endosteal cortical borders were semi-manually identified on
each histology image using ImageJ software (NIH) by an experienced bone
histologist (AA) (Dominguez & Agnew, 2019). These were used as gold stan-
dard cortical bone cross-sectional geometries at their specific rib locations,
and each histology image was spatially registered within its corresponding
CT image volume as follows. Firstly, rigid registration errors were calcu-
lated between the histology-derived periosteal border and those taken from
successive cross-sectional cuts through an initial CT-derived periosteal sur-
face (described below). Local minima in registration error indicated strongly
matching regions, and visual overlays of the histology image onto the CT vol-
ume were used for minor adjustment to align cortices and trabeculae between
the two modalities. A typical overlay is presented in Figure 2 showing the
local patterns of trabecular bone—clearly visible on histology and slightly
blurred on CT—in strong alignment. For all cut histology sections, the loca-

6

tion in CT image space (along the rib's length) of minimum rigid registration
error occurred near to the corresponding physical fracture location that was
noted by hand. In all cases the final chosen position that showed the strongest
coherence in trabecular patterns between histology and CT was less than 1 %
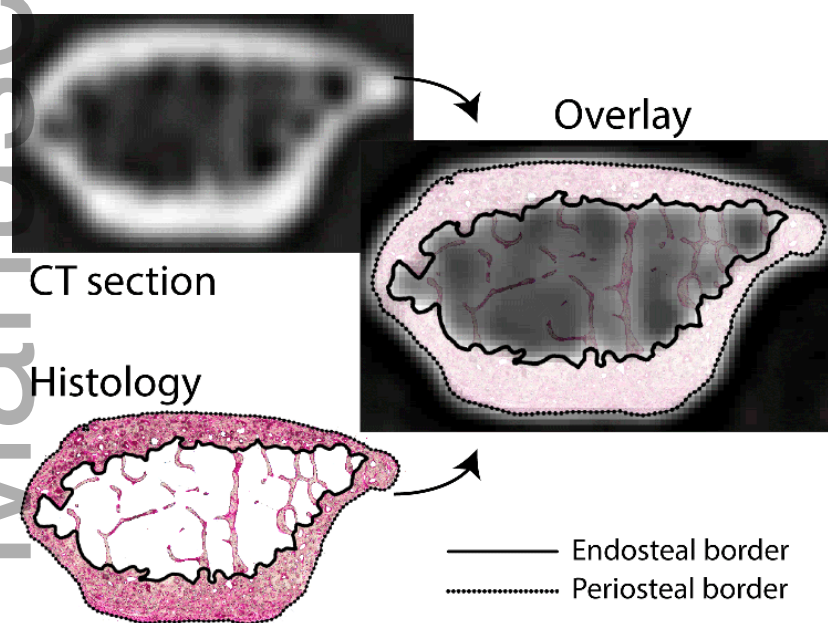in rib length from the position exhibiting minimum rigid registration error.

Figure 2: Exemplar histology image overlay showing the spatial correspondence to the
underlying CT image volume at each chosen cross-sectional position.

2.2. CT image processing

An initial and approximate 3D periosteal surface was generated from each
rib's CT volume via segmentation performed in MIMICS (v19, Materialise).
All subsequent image and statistical analyses were performed in MATLAB
(The Mathworks). A central axis along the rib was formed from the rib head
(at the vertebral or posterior end) to its sternal (or anterior) end by fitting

7

a smoothed spline through the 2D centroids obtained from successive cross-sectional cuts across this initial periosteal surface. This initial surface was then discretized along the central axis into 301 successive and equally spaced cross-sections. Each section was further discretized to 80 locations around its circumference to produce an overall surface map as depicted in Figure 3.
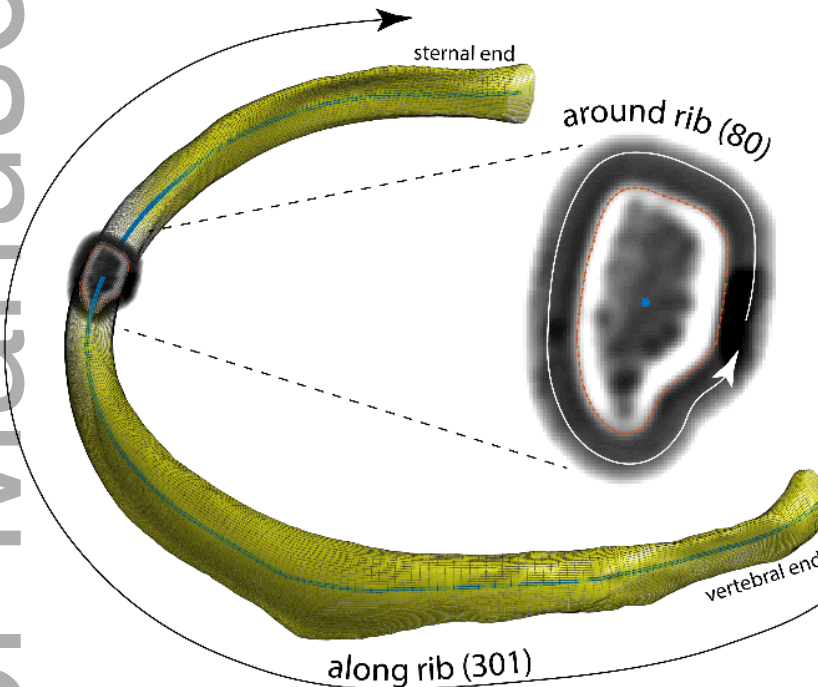

Figure 3: Ribs are discretized to a 301 (along) by 80 (around) grid of rib surface locations.

Local pleural and cutaneous aspects for each cross-section were calculated using the two points on its circumference intersected by that section's minor inertial axis. A smoothed spline fitted to these points formed overall rib pleural and cutaneous aspects. Co-alignment between rib surface maps was achieved by aligning the circumferential locations along these aspects.

At each surface location (that is, at 301×80 locations per rib), a 1D

8

cortical signal of the image intensity across the cortex was produced by re-

sampling the underlying CT image in a direction normal to the 3D surface at that location. The Cortical Bone Mapping method (CBM) was then applied to each cortical signal. CBM uses nonlinear optimization to match a model consisting of three constant density regions (y_0 outside the periosteal border, y_1 within the cortex, and y_2 inside the endosteal border) to the cortical signal. The distance between the optimally-fitted periosteal and endosteal estimates (x_0 and x_1) provides the local cortical bone thickness, and the collection of individual estimates across a rib's gridded surface provide overall rib thickness maps. As per previous work (Holcombe et al., 2018; Treece et al., 2010) the cortical density model parameter (y_1) was fixed within each CBM optimization to a Hounsfield unit value corresponding to the density seen in the thickest bone region along the rib, and weighting was applied to more aggressively penalize model fitting errors located near the initial periosteal surface.

In this study, additional error-based local smoothing was applied to the collected x_0 and x_1 value maps using a 0.3 mm Gaussian-shaped smoothing kernel that was further scaled by the inverse of the CBM model fitting error at those same locations. This step served to reduce high-frequency noise in resulting border locations across the rib surfaces and also reduced the influence of poorly-fitted individual cortical signals.

Finally, filters were used to suppress potentially misleading thickness measurements within a given cross-section as described in Holcombe et al. (2018) and summarized below. Firstly, individual signals wherein the parameters from the CBM method's optimization step did not converge to internal (non-

9

₁₄₂ boundary) values were ignored. Secondly, morphological criteria applied to each circumferential ring of estimated endosteal borders were used to dis-
₁₄₄ card signals which did not pass through a single isolated cortical wall. This is most commonly seen near areas of high local curvature such as the costal
₁₄₆ groove.

2.2.1. Geometric measurements

₁₄₈ Overall, the steps above served to produce an underlying 301×80 map of local cortical bone thickness (CT.TH) estimates obtained from CT, with one
₁₅₀ map for each of the 33 whole ribs. These maps were averaged to produce an average CT.TH map for the study population.

₁₅₂ Additionally, the sequence of periosteal and endosteal border positions around each individual cross-section were joined to produce the geometric
₁₅₄ shape of that section's predicted cortical shell (for 301 shells per rib). Cross-sectional geometry measurements of each of these shells were calculated, con-
₁₅₆ sisting of the total sub-periosteal area (TT.AR), the cortical area (CT.AR), the endosteal area (ES.AR), and the cortical shell's maximal (or principal)
₁₅₈ and minimal (or secondary) area inertial moments (IMAX, and IMIN). The IMAX and IMIN inertial axes intersect the 2D centroid of the cortical shell
₁₆₀ and, with rib cross-sections generally elongated, the IMAX inertial axis occurs along an approximately inferior to superior aspect while the IMIN inertial
₁₆₂ axis lies perpendicular to IMAX along a pleural to cutaneous aspect. As a descriptor of rib cross-sectional aspect ratio, IRAT was calculated as IMAX
₁₆₄ divided by IMIN. The six overall cross-sectional measurements were grouped by position along a rib to report population average values and a $\pm$1SD pop-
₁₆₆ ulation corridor, each calculated as a function of position from the vertebral

10

rib end to the sternal rib end.

Regional sex-based differences in bone thickness and in cross-sectional geometry measurement distributions were assessed via two-sample t-tests with significance determined at the $p < 0.05$ level.

2.3. Validation against histology

Each histological image ($N = 39$) matched a specific cross-sectional position along the length of one of the 33 whole ribs. A CT validation set was produced by using gold standard measurements obtained directly from the periosteal and endosteal borders drawn on the histology images, and pairing them with measurements from the spatially equivalent locations within the full CT image volumes of the same ribs. Therefore, the validation set for all CT measurements consisted of 3120 local cortical bone thickness (CT.TH) measurement pairs (at 80 locations around each of 39 sections), and 39 pairs (one per histology image section) for the TT.AR, CT.AR, ES.AR, IMAX, IMIN, and IRAT rib cross-sectional shape measurements. Additionally, the difference in principal inertial axis orientation (IANG) between the cortical shell shapes obtained using CT and histology was calculated. For IANG, a positive difference indicated rotational misalignment (having the superior rib aspect rotate towards the pleural side) of the cortical shell obtained using CT compared to the target cortical shell from histology.

Individual thickness values discarded via the morphological filters described above were excluded from the CT.TH validation set, and their border positions were linearly interpolated via neighboring successful measurements in order to provide complete cross-sectional geometry. For all measurement

11

pairs in the validation set, the measurement accuracy (mean error) and precision (SD error) of CT-based predictions was calculated.

3. Results

3.1. Accuracy assessment

From 3120 histology-matched cortical bone signal locations (at 80 locations sampled around each of the 39 sections with histology), 37 signals did not converge adequately during CBM optimization and 161 were identified by morphological filters as not falling across a clear singular cortex. The remaining 2922 (94 %) predictions of Ct.Th from CT for comparison to gold standard values from their histology-based pairs, are shown as scattered data in Figure 4.

Overall accuracy (mean error) and precision (SD error) of predicted cortical thickness values from CT ($N = 2922$) was -0.013 ± 0.167 mm, and Table 1 also lists the accuracy and precision for CT-based predictions of each of the full cross-sectional property measurements ($N = 39$). In general, cross-sectional property predictions were well correlated with gold standard values ($R^2 > 0.91$ for all properties), but with CT-based predictions on average overestimating area properties by 0.1 % (Ct.Ar), 4.7 % (Tt.Ar), and 6.8 % (Es.Ar).

3.2. Sectional property variation

Average values and 1SD male and female corridors for regional Ct.Ar, Tt.Ar, Es.Ar, Imax, Imin, and Irat are shown in Figure 5, and all corridor data is included as supplementary information. Specifically, male ribs
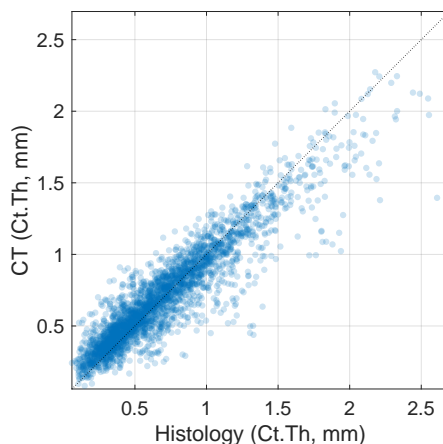
12

Figure 4: Predicted individual thickness measurements compared to spatially equivalent measures from histology (coefficient of determination $R^2 = 0.84$, $p < 0.0001$).

had significantly larger (at the $p < 0.05$ level) CT.AR at 56 % of rib locations, and significantly larger TT.AR, ES.AR, ES.AR, IMAX, and IMIN at over 96 % of rib locations. Inertial aspect ratio (IRAT) varied along the rib with local peaks in aspect ratio occurring near either rib end and within a region spanning approximately 25 % to 50 % of the rib's length. This region corresponds to the greatest prominence of the rib's costal groove, and here female ribs were significantly more elongated than male ribs whereas rib aspect ratios in other regions were not significantly different. As seen on Figure 5, the maximal CT.AR along the length of the rib occurs near the rib tubercle (approximately 10 % rib length) and decreases steadily towards the sternal end, whereas TT.AR remains relatively constant across most of a rib's length before increasing sharply towards its sternal end. These cross-sectional changes along a rib's length are visualized in Figure 6 which shows the CT predictions of cortical bone borders for a number of subjects and rib

13

Table 1: Values from gold standard histology and their predictions errors from CT (mean±SD) for Cᴛ.Tʜ (N = 2922) and whole rib section properties (N = 39), with coefficients of determination (R^2) from linear regression ($p < 0.0001$ for all models)

| | Histology | CT | | |
| | mean $\pm$ SD | mean $\pm$ SD | Pred. Error | R^2 |
Measure				
Cᴛ.Tʜ (mm)	0.7 ± 0.4	0.7 ± 0.3	-0.013 ± 0.167	0.84
Cᴛ.Aʀ (mm^2)	20.4 ± 8.0	20.4 ± 6.3	0.03 ± 2.67	0.91
Tᴛ.Aʀ (mm^2)	64.1 ± 20.8	67.1 ± 21.5	3.00 ± 1.16	1.00
Es.Aʀ (mm^2)	43.7 ± 17.1	46.7 ± 18.2	2.97 ± 2.54	0.98
Iᴍᴀx (mm^4)	247.5 ± 160.3	262.8 ± 151.6	15.34 ± 42.69	0.93
Iᴍɪɴ (mm^4)	124.0 ± 86.5	132.7 ± 82.8	8.61 ± 14.44	0.97
Iʀᴀᴛ	2.2 ± 0.9	2.2 ± 0.9	-0.04 ± 0.14	0.98
Iᴀɴɢ (deg.)			0.63 ± 2.45	

locations, and highlights the overall inter-subject and intra-subject variability in rib cross-sectional geometry.

3.3. Cortical bone thickness maps

The full rib cortical bone thickness map (Cᴛ.Tʜ) was calculated for each rib, and the resulting average Cᴛ.Tʜ map from the full sample is shown in Figure 7. Accumulating all rib locations together, males and females had average±SD Cᴛ.Tʜ values of 0.71 ± 0.35 mm and 0.76 ± 0.38 mm, respectively. Assessing on a regional basis, the majority (90.4 %) of rib surface locations did not show a significant difference ($p > 0.05$) in cortex thickness between males and females. Therefore, Cᴛ.Tʜ thickness maps have been shown using pooled data from both sexes. This pooled Cᴛ.Tʜ map along-
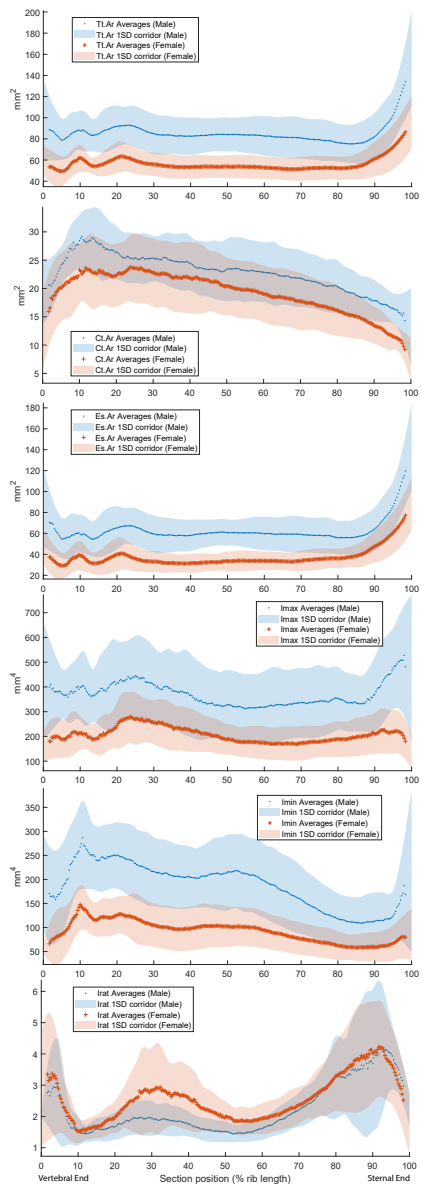
14

Figure 5: Measurements by sex of rib cross-sectional total area (Tᴛ.Aʀ), cortical bone area (Cᴛ.Aʀ), endosteal area (Eꜱ.Aʀ), primary and second inertial moments (Iᴍᴀx, Iᴍɪɴ) and Iᴍᴀx/Iᴍɪɴ inertial moment ratio (Iʀᴀᴛ) as a function of cross-section location from the vertebral (0%) to sternal (100%) rib ends.
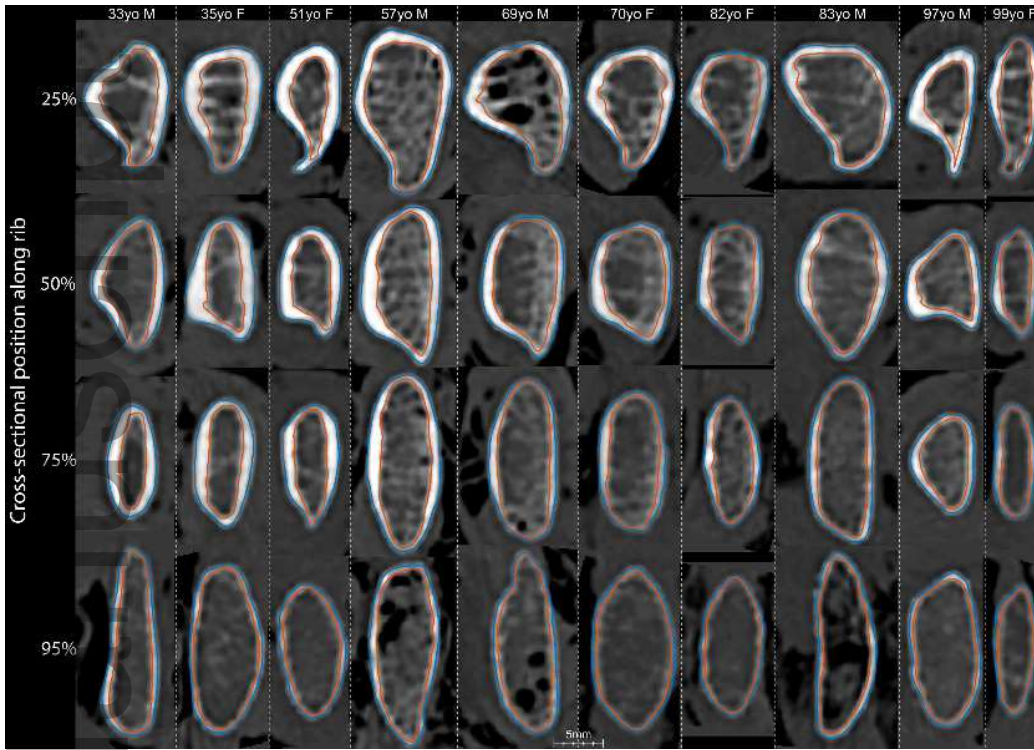
15

Figure 6: Exemplar cross-sections through CT volumes showing the predicted periosteal (outer) and endosteal (inner) cortical border using a range of male and female subjects (see upper labels) and rib locations (see left labels).

side separated male and female average maps are provided as supplementary information.

4. Discussion

Here we have assessed detailed rib cortical bone thickness and cross-sectional geometry from 33 adult sixth ribs. Starting with an initial approximate rib segmentation, the CBM method was applied using error-weighted smoothing and morphological filters, and average cortical bone thickness

16
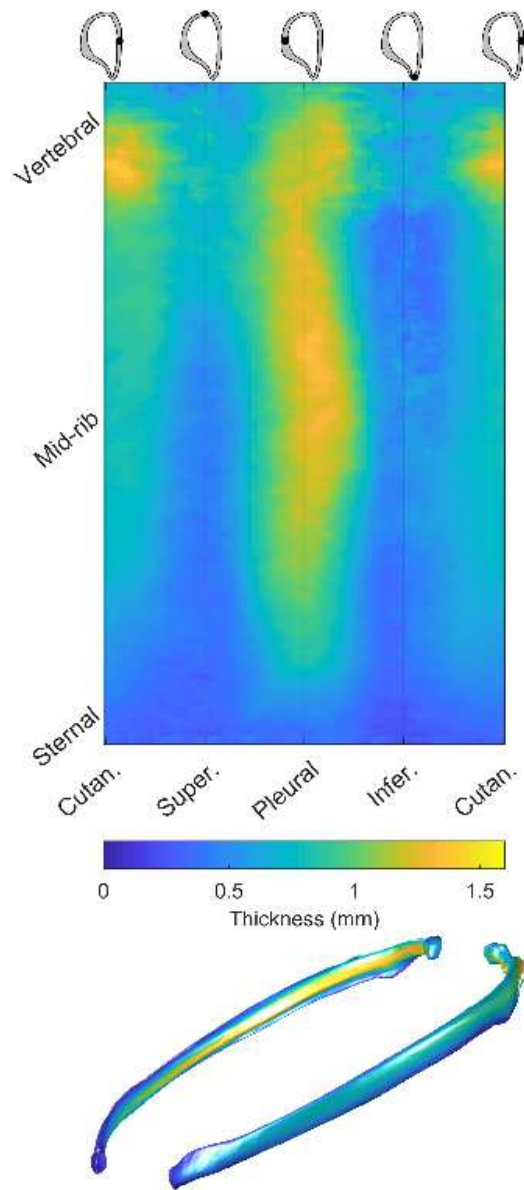
Figure 7: The average rib cortical bone thickness map in gridded form (above) and projected onto exemplar subject geometry (below).

246 maps and cross-sectional property 1SD corridors for males and females have been presented.

17

The measurement techniques used in this study are similar to those presented in Holcombe et al. (2018) with adjustments to allow for full rib image volumes rather than individual rib section images. The image volumes in the current study have $0.15 \times 0.15 \times 0.67$ mm voxels, providing resolutions that are both higher (in-plane directions) and lower (out-of-plane direction) than the highest resolution images of 0.37 mm/pixel used in Holcombe et al. (2018). Correspondingly, the current accuracy and precision of measurement predictions from CT are largely similar to those from this previous study which found prediction errors of -0.03 ± 0.17 mm for CT.TH, -0.6 ± 1.5 mm^2 for CT.AR, and 2.1 ± 1.5 mm^2 for TT.AR.

For measuring cross-sectional rib properties using CT, the current CBM-based methodology is more accurate than traditional CT thresholding methods, which often overestimate the amount of bone in a given cross-section. Perz et al. (2015) found that simple histogram-based thresholding of CT images resulted in average errors in TT.AR of $8 \pm 3\%$, while Murach et al. (2017) used an adaptive histogram-based thresholding technique on 19 CT images of similar resolution to the current study, finding TT.AR errors of $3 \pm 11\%$. Those same studies reported that their CT thresholding techniques produced unacceptable CT.AR overestimations of $40 \pm 12\%$ and $71 \pm 45\%$, respectively. In the current study we see similar or improved accuracy and precision in TT.AR with errors of $4.7 \pm 1.8\%$, and greatly reduced errors of $0.1 \pm 13.1\%$ for CT.AR. It is informative to note that the initial periosteal border in the current study—obtained using a standard 226 HU threshold for bone segmentation—also overestimated TT.AR on these same images by $21 \pm 4\%$.

18

4.1. Sex-based sectional differences

Results highlighted in Figure 5 show that while there are similar trends in average rib cross-sectional properties along the lengths of male and female ribs, there were significant sex-based differences in their magnitudes with males ribs being larger in terms of all area and inertial measurements and at a large majority of positions along those ribs. Comparing results for CT.TH, on the other hand, sex-based differences were less pronounced with male ribs having significantly thicker cortices at just 2.1 % of rib surface locations (at the $p < 0.05$ level), and female ribs having thicker cortices at 7.5 % of rib surface locations. Taken together, these results do indicate that the larger CT.AR seen in males is primarily due to males having larger overall cross-sectional size to their ribs than females rather than males having rib bones with thicker cortices than females. Notably also, female subjects in this study were on average older (but not significantly older) than the males, and bone quantity in general is known to decrease with age. However, (Agnew et al., 2018) found no significant decrease in average pleural or cutaneous CT.TH with age (or by sex) on a large sample of ribs, suggesting age is likely not a confounding factor here.

As seen in Figure 5, the rib cross-sectional position of highest CT.AR is near the rib tubercle (approximately 10 % rib length), and a steady reduction in CT.AR is seen from this location towards the sternal end. Rib TT.AR, however, remains relatively constant across most of a rib's length before increasing sharply towards its sternal end, despite variability in the qualitative shape seen in Figure 6. Each of these observations match findings by Choi & Kwak (2011) who measured cross-sectional areas from ribs of seven elderly

19

male cadaveric ribs. While not reporting sixth rib data, their fifth rib results showed an average Tt.Ar of $91\,\text{mm}^2$ that was constant from the tubercle to $90\,\%$ of the rib's length, and a drop in Ct.Ar across that same region from $26\,\text{mm}^2$ to $19\,\text{mm}^2$. Each of these fall within the 1SD male corridors obtained from the current study.

4.2. Cortical bone thickness map

Consistent patterns in cortical bone thickness maps were also seen across individuals, as typified by the population average map (Figure 7). Beyond the tubercle, all ribs showed local Ct.Th maxima along the pleural and cutaneous aspects and local Ct.Th minima along the superior and inferior aspects, with these features lessening at the most sternal end of the rib to form uniformly thin cortices like those seen at the 95th percentile position in Figure 6. The pleural aspect contained the thickest regions of bone, with Ct.Th values peaking to between $0.9\,\text{mm}$ to $2.6\,\text{mm}$ across the population at approximately mid-rib locations.

4.3. Thickness map registration

When performing statistical aggregation it is important that variable sets (in this case individual thickness maps) are spatially registered to maintain correspondence between regions on the maps from different individuals. The one-dimensional registration along the length of the rib is straightforward whereby sample locations are equally spaced along the rib's central axis from the vertebral to sternal rib ends. In this study the further registration of rotational positions around the ribs are based only on the surface geometry of the ribs. We have taken the general approach of positioning the pleural and

20

cutaneous registration aspects at locations where the rib section's secondary inertial axis intersects with its periosteal border. For continuity, these locations were calculated at each cross-section and a smoothing spline was fitted to provide their exact location.

Having registration depend only on rib surface geometry means that local features of the thickness maps themselves (which are a product of external and internal surface geometries) are not explicitly aligned. For example, all ribs in this study were seen to have a regional maxima along or near their pleural margin. Yet, these regional maxima did not align precisely to the pleural position as determined by only that rib's surface geometry.

It would be desirable to have the regional maximum from the average thickness map correspond to the average regional maxima from each constituent rib map. In the current study, the average thickness map registered by surface features alone actually underestimated the average of the regional maxima along the mid-rib pleural aspect by approximately 0.06 mm (5 %). Similarly, the regional minima at the superior aspect of the mid-to-sternal portion rib was overestimated by approximately 10 % compared to the collection of minima from each individual thickness map.

4.4. Limitations

A primary limitation of the current study is that its results are presented only for sixth level ribs. With ribs of different levels in the rib cage serving different mechanical roles, it is expected that both global and local anatomies will differ accordingly. Indeed, ribs do differ by level in terms of global size and shape (Holcombe et al., 2017; Wang et al., 2016; Weaver et al., 2014), overall mechanical stiffness Kindig et al. (2011), and local cross-section (Choi

21

& Kwak, 2011; Wang et al., 2016). Nevertheless, the combination of CT and

348 histological image modalities used in this study allows us to establish methods for validating the typical full-rib properties of this mid-level rib.

350 This reference at the sixth rib level can be used to verify that future measurements—which may be obtained from sources such as clinical CT

352 scans with less optimal imaging characteristics and without recourse to gold standards for validation—are free of systematic bias due to their particular

354 imaging conditions.

The current study population covered a wide age range with the inten-

356 tion that average results are seen as typical of an adult (US) population. In measures where significant sex-based differences were found we have cho-

358 sen to provide male and female results separately. Future work should aim to broaden the subject population to include children, and to increase the

360 subject count so as to allow statistical analyses that incorporate other demographic factors such as age, stature, body mass, and ancestry.

362 *4.5. Applications and Future Work*

The technique outlined in this study can be used to create accurate rib

364 endosteal and periosteal surfaces along the entire length of the rib, which can improve simulation efforts greatly. The rib cortical bone thickness ref-

366 erence data used in current human body models is limited in terms of the population from which it was drawn, and in terms of the geometric detail

368 that it provides. Li et al. (2010) demonstrated the positive effects of including more specific cortical thickness variation into simulation studies, and

370 Agnew et al. (2018) quantified the significant effect that cross-sectional geometry has on ribs resistance to loading from physical tests. These studies

22

have demonstrated the need for more advanced approaches to understanding human variation in rib properties and differential rib fracture risk between individuals.

Future work can target the improvement of HBMs by incorporating the results obtained here for cortical bone thickness maps into HBM rib definitions. Future efforts can also assess the geometric accuracy of such models, testing their ability to represent their target population by comparing their modeled rib geometries to the typical adult corridors published here.

5. Conclusion

Numerical models are an important tool for understanding and preventing traumatic injuries to the chest, and the ribs form a key structural model component. Models are typically developed using CT image data, but traditional CT segmentation methods have been inadequate for obtaining accurate cortical bone geometry. As such, only simplified cortex data has been applied based on limited available literature from higher resolution sources.

Here we have applied a Cortical Bone Mapping (CBM) methodology to whole human ribs, assessed the accuracy of these techniques against gold standard measurements from histology, and presented detailed population-based data for rib cortical bone thickness and for rib cross-sectional properties. The population data presented here for rib cortical bone thickness and cross-sectional area can be used directly to assess and improve the veracity of current FE models of human ribs. Finally, results here can validate future steps towards personalized and population-based geometry of human ribs from more broadly sampled yet less detailed image data such as live-subject

23

clinical CT scans.

Disclosures

The authors report that there are no conflicts of interest which might affect this work.

Acknowledgements

References

References

Agnew, A. M., Moorhouse, K., Kang, Y.-S. S., Donnelly, B. R., Pfeferle, K., Manning, A. X., Litsky, A. S., Herriott, R., Abdel-Rasoul, M., & Bolte, J. H. (2013). The response of pediatric ribs to quasi-static loading: mechanical properties and microstructure. *Annals of Biomedical Engineering*, *41*, 2501–2514. URL: http://dx.doi.org/10.1007/s10439-013-0875-6. doi:10.1007/s10439-013-0875-6.

Agnew, A. M., Murach, M. M., Dominguez, V. M., Sreedhar, A., Misicka, E., Harden, A., Bolte, J. H., Kang, Y.-S., Stammen, J., & Moorhouse, K.

24

(2018). Sources of variability in structural bending response of pediatric and adult human ribs in dynamic frontal impacts. *Stapp car crash journal*, *62*.

Choi, H. Y., Han, J., Park, Y., & Yoon, K. H. (2009). Digital elderly human body modeling. URL: `http://dx.doi.org/10.4271/2009-01-2262`. doi:`10.4271/2009-01-2262`.

Choi, H.-Y., & Kwak, D.-S. (2011). Morphologic characteristics of korean elderly rib. *J. Automot. Saf. Energy*, *2*.

Dominguez, V. M., & Agnew, A. M. (2019). The use of roi overlays and a semi-automated method for measuring cortical area in imagej for histological analysis. *American journal of physical anthropology*, *168*, 378–382.

Gayzik, F. S., Moreno, D. P., Geer, C. P., Wuertzer, S. D., Martin, R. S., & Stitzel, J. D. (2011). Development of a full body CAD dataset for computational modeling: A multi-modality approach. *Annals of Biomedical Engineering*, *39*, 2568–2583. URL: `http://dx.doi.org/10.1007/s10439-011-0359-5`. doi:`10.1007/s10439-011-0359-5`.

Holcombe, S. A., Hwang, E., Derstine, B. A., & Wang, S. C. (2018). Measuring rib cortical bone thickness and cross section from CT. *Medical Image Analysis*, *49*, 27–34. URL: `http://dx.doi.org/10.1016/j.media.2018.07.003`. doi:`10.1016/j.media.2018.07.003`.

Holcombe, S. A., Wang, S. C., & Grotberg, J. B. (2016). The effect of rib shape on stiffness. *Stapp Car Crash Journal*, *60*, 11–24. URL: `http://view.ncbi.nlm.nih.gov/pubmed/27871092`.

25

Holcombe, S. A., Wang, S. C., & Grotberg, J. B. (2017). The effect of age and demographics on rib shape. *Journal of Anatomy*, *231*, 229–247. URL: `http://dx.doi.org/10.1111/joa.12632`. doi:`10.1111/joa.12632`.

Ito, O., Dokko, Y., & Ohashi, K. (2009). Development of adult and elderly FE thorax skeletal models. URL: `http://dx.doi.org/10.4271/2009-01-0381`. doi:`10.4271/2009-01-0381`.

Kemper, A. R., McNally, C., Pullins, C. A., Freeman, L. J., Duma, S. M., & Rouhana, S. M. (2007). The biomechanics of human ribs: material and structural properties from dynamic tension and bending tests. *Stapp Car Crash Journal*, *51*, 235–273. URL: `http://view.ncbi.nlm.nih.gov/pubmed/18278600`.

Kindig, M., Lau, A. G., & Kent, R. W. (2011). Biomechanical response of ribs under quasistatic frontal loading. *Traffic Injury Prevention*, *12*, 377–387. URL: `http://dx.doi.org/10.1080/15389588.2011.583960`. doi:`10.1080/15389588.2011.583960`.

Li, Z., Kindig, M. W., Subit, D., & Kent, R. W. (2010). Influence of mesh density, cortical thickness and material properties on human rib fracture prediction. *Medical Engineering & Physics*, *32*, 998–1008. URL: `http://dx.doi.org/10.1016/j.medengphy.2010.06.015`. doi:`10.1016/j.medengphy.2010.06.015`.

Mayeur, O., Chaari, F., Delille, R., Guillemot, H., & Drazetic, P. (2010). A new method to determine rib geometry for a personalised FEM of the thorax. In *Proceedings of International IRCOBI Conference* (pp. 235–246).

26

Mohr, M., Abrams, E., Engel, C., Long, W. B., & Bottlang, M. (2007). Geometry of human ribs pertinent to orthopedic chest-wall reconstruction. *Journal of Biomechanics*, *40*, 1310–1317. URL: `http://dx.doi.org/10.1016/j.jbiomech.2006.05.017`. doi:`10.1016/j.jbiomech.2006.05.017`.

Murach, M. M., Kang, Y.-S., Bolte, J. H., Stark, D., Ramachandra, R., Agnew, A. M., Moorhouse, K., & Stammen, J. (2018). Quantification of skeletal and soft tissue contributions to thoracic response in a dynamic frontal loading scenario. *Stapp car crash journal*, *62*.

Murach, M. M., Kang, Y.-S., Goldman, S. D., Schafman, M. A., Schlecht, S. H., Moorhouse, K., Bolte, J., & Agnew, A. M. (2017). Rib geometry explains variation in dynamic structural response: Potential implications for frontal impact fracture risk, . (pp. 1–15). URL: `http://dx.doi.org/10.1007/s10439-017-1850-4`. doi:`10.1007/s10439-017-1850-4`.

Okoukoni, C., Lynch, S. K., McTyre, E. R., Randolph, D. M., Weaver, A. A., Blackstock, A. W., Lally, B. E., Munley, M. T., & Willey, J. S. (2016). A cortical thickness and radiation dose mapping approach identifies early thinning of ribs after stereotactic body radiation therapy. *Radiotherapy and Oncology*, *119*, 449–453. URL: `http://dx.doi.org/10.1016/j.radonc.2016.03.023`. doi:`10.1016/j.radonc.2016.03.023`.

Perz, R., Toczyski, J., & Subit, D. (2015). Variation in the human ribs geometrical properties and mechanical response based on x-ray computed tomography images resolution. *Journal of the Mechanical Behavior of*

27

486 *Biomedical Materials*, *41*, 292–301. URL: http://dx.doi.org/10.1016/
j.jmbbm.2014.07.036. doi:10.1016/j.jmbbm.2014.07.036.

488 Schoell, S. L., Weaver, A. A., Vavalle, N. A., & Stitzel, J. D. (2015). Age-
and Sex-Specific thorax finite element model development and simulation.
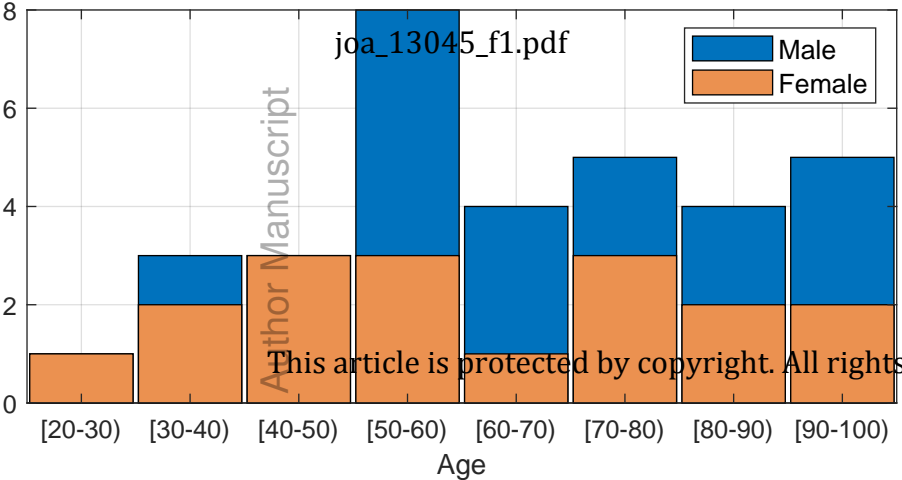490 *Traffic Injury Prevention*, *16*, S57–S65. URL: http://dx.doi.org/10.
1080/15389588.2015.1005208. doi:10.1080/15389588.2015.1005208.

492 Sirmali, M., Türüt, H., Topçu, S., Gülhan, E., Yazici, U., Kaya, S., &
Taştepe, I. (2003). A comprehensive analysis of traumatic rib fractures:
494 morbidity, mortality and management. *European journal of cardio-thoracic
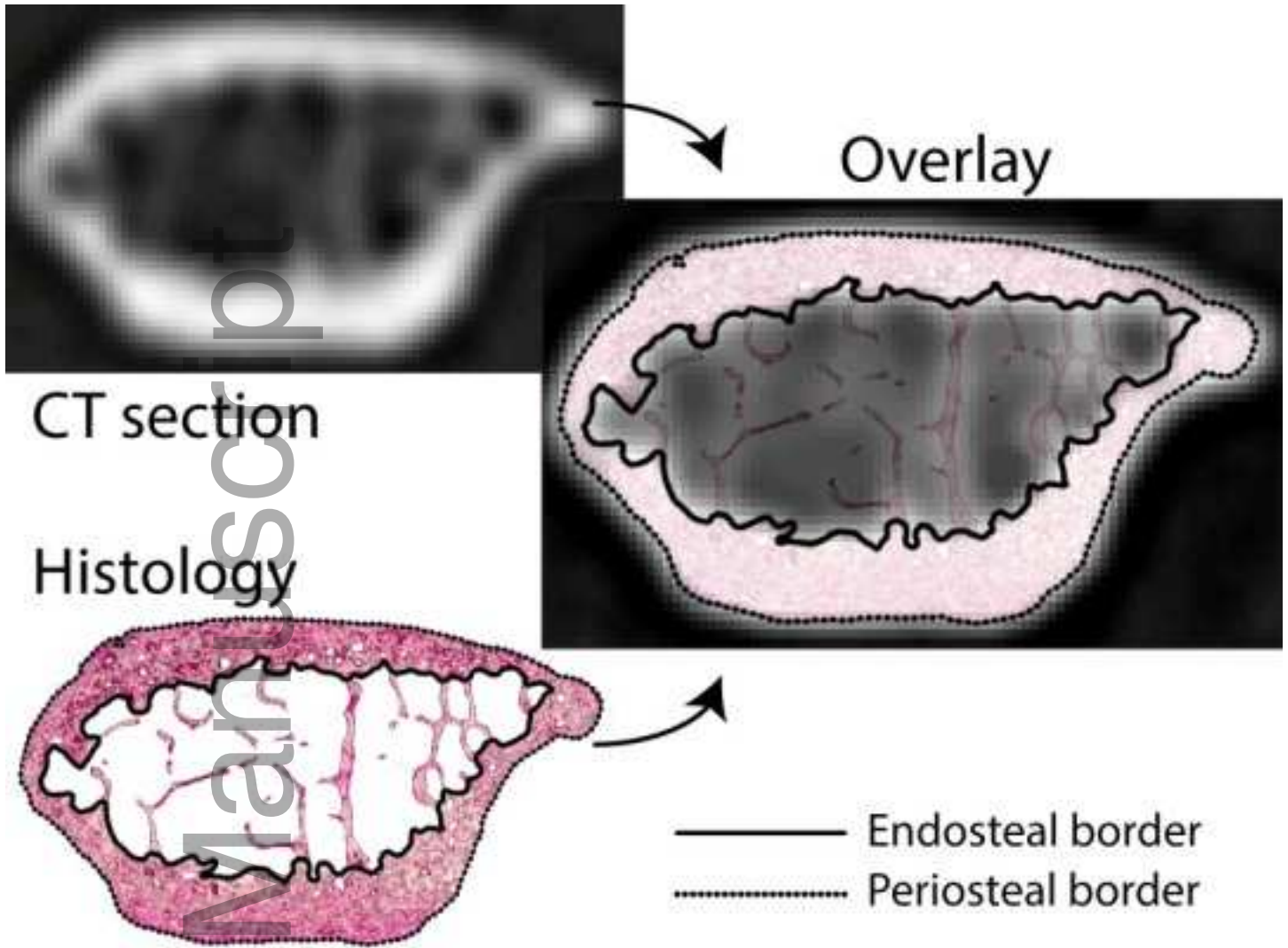surgery*, *24*, 133–138. URL: http://view.ncbi.nlm.nih.gov/pubmed/
496 12853057.

Stawicki, S. P., Grossman, M. D., Hoey, B. A., Miller, D. L., & Reed, J. F.
498 (2004). Rib fractures in the elderly: A marker of injury severity. *Journal of
the American Geriatrics Society*, *52*, 805–808. URL: http://dx.doi.org/
500 10.1111/j.1532-5415.2004.52223.x. doi:10.1111/j.1532-5415.2004.
52223.x.

502 Stein, I. D. (1976). Rib structure and bending strength: an autopsy
study. *Calcified Tissue Research*, *20*, 61–73. URL: http://dx.doi.org/
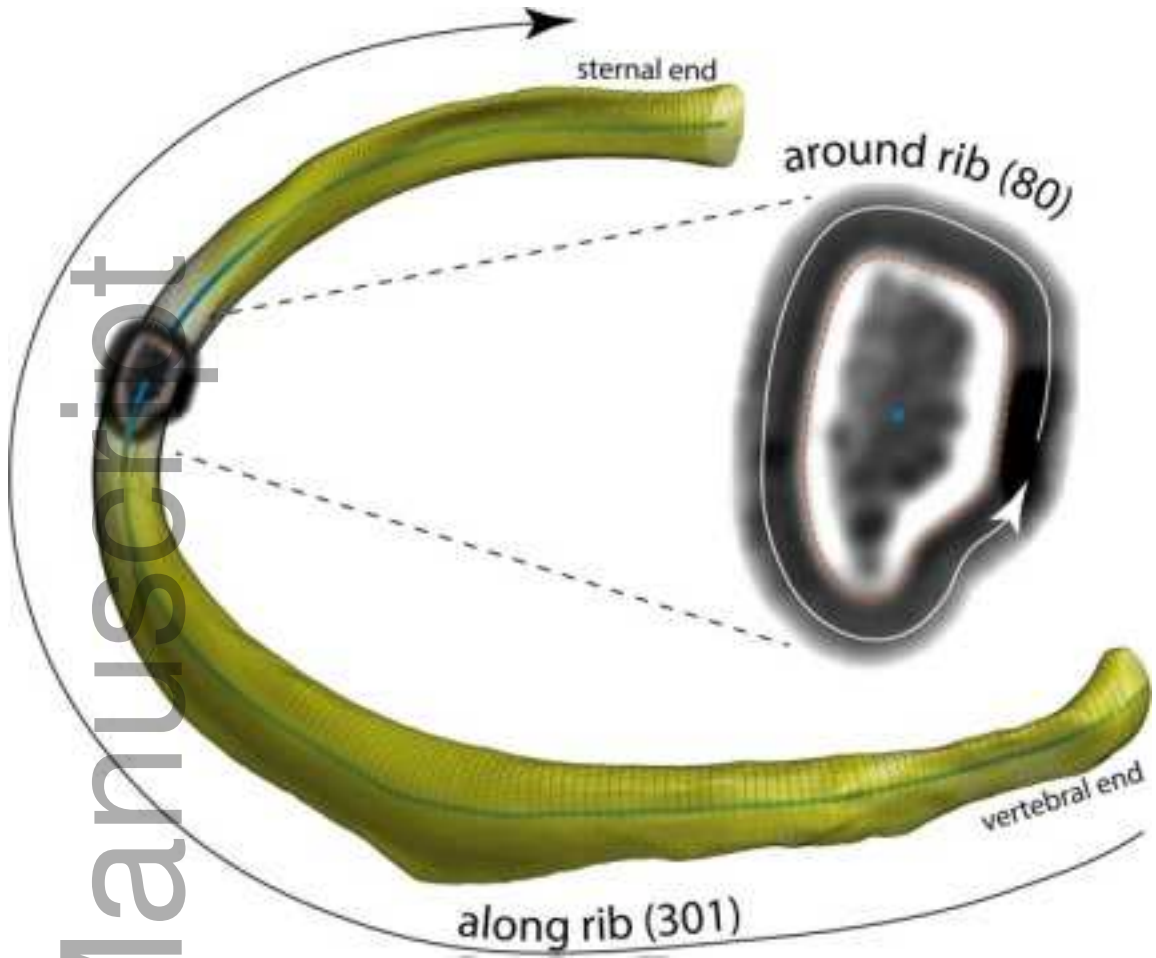504 10.1007/BF02546398. doi:10.1007/BF02546398.

Treece, G. M., & Gee, A. H. (2015). Independent measurement of femoral
506 cortical thickness and cortical bone density using clinical CT. *Medical Im-
age Analysis*, *20*, 249–264. URL: http://dx.doi.org/10.1016/j.media.
508 2014.11.012. doi:10.1016/j.media.2014.11.012.

28

Treece, G. M., Gee, A. H., Mayhew, P. M., & Poole, K. E. S. (2010). High res-
olution cortical bone thickness measurement from clinical CT data. *Medi-
cal Image Analysis*, *14*, 276–290. URL: `http://dx.doi.org/10.1016/j.`
`media.2010.01.003`. doi:`10.1016/j.media.2010.01.003`.

Wang, Y., Cao, L., Bai, Z., Reed, M. P., Rupp, J. D., Hoff, C. N., & Hu,
J. (2016). A parametric ribcage geometry model accounting for variations
among the adult population. *Journal of Biomechanics*, *49*, 2791–2798.
URL: `http://dx.doi.org/10.1016/j.jbiomech.2016.06.020`. doi:`10.`
`1016/j.jbiomech.2016.06.020`.

Weaver, A. A., Schoell, S. L., & Stitzel, J. D. (2014). Morphometric analysis
of variation in the ribs with age and sex. *Journal of Anatomy*, *225*, 246–
261. URL: `http://dx.doi.org/10.1111/joa.12203`. doi:`10.1111/joa.`
`12203`.

Wuermser, L.-A., Achenbach, S. J., Amin, S., Khosla, S., & Melton, L. J.
(2011). What accounts for rib fractures in older adults? *Journal of Os-
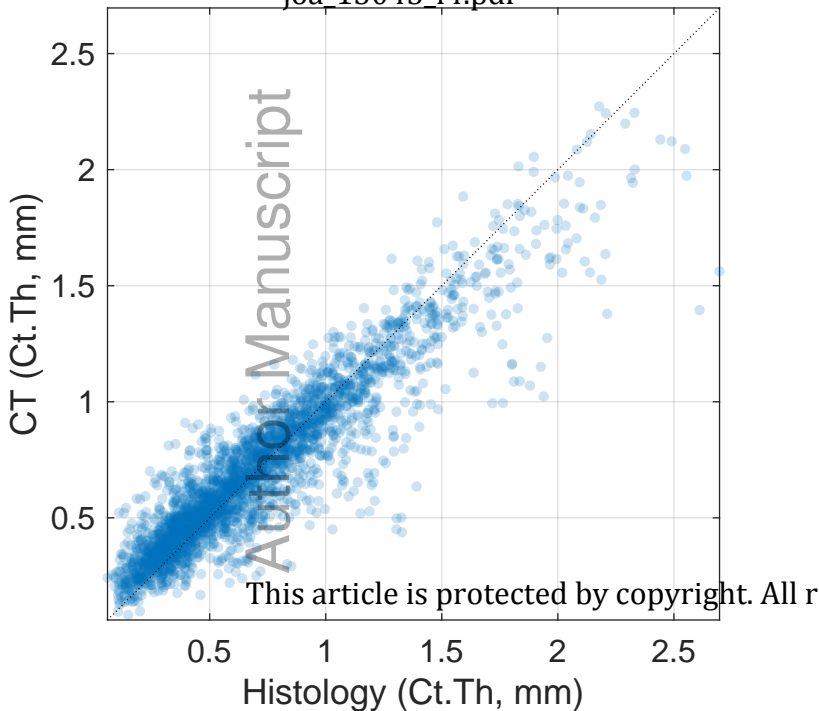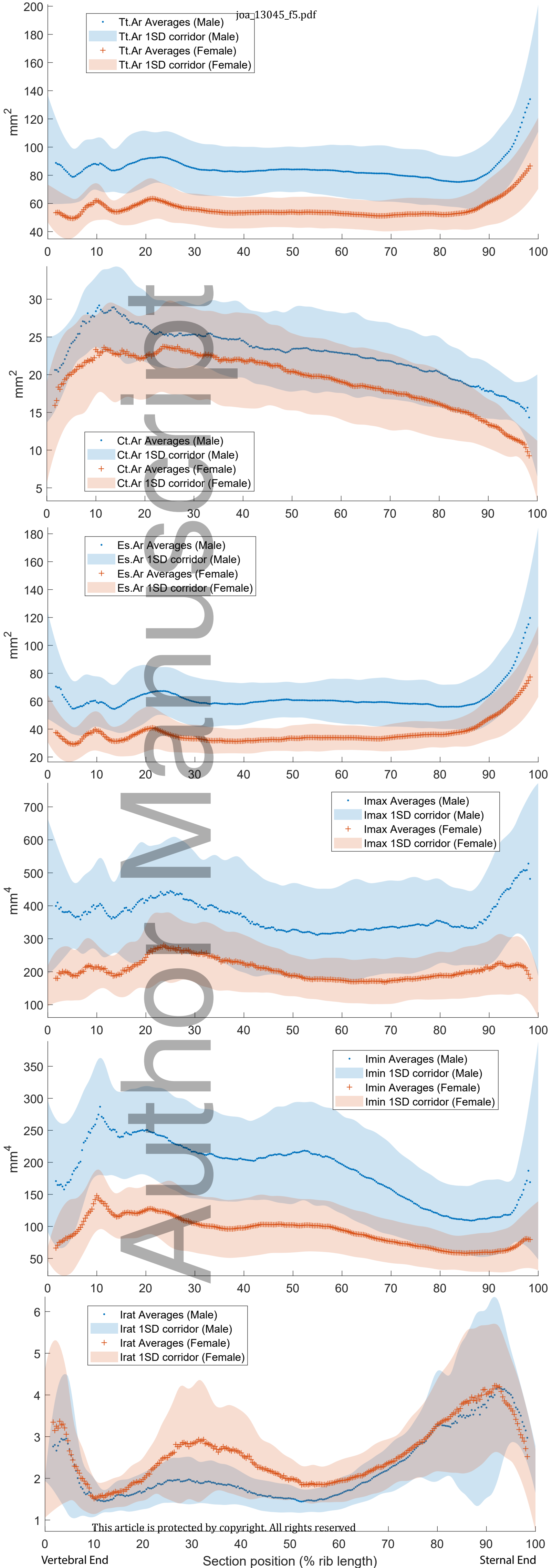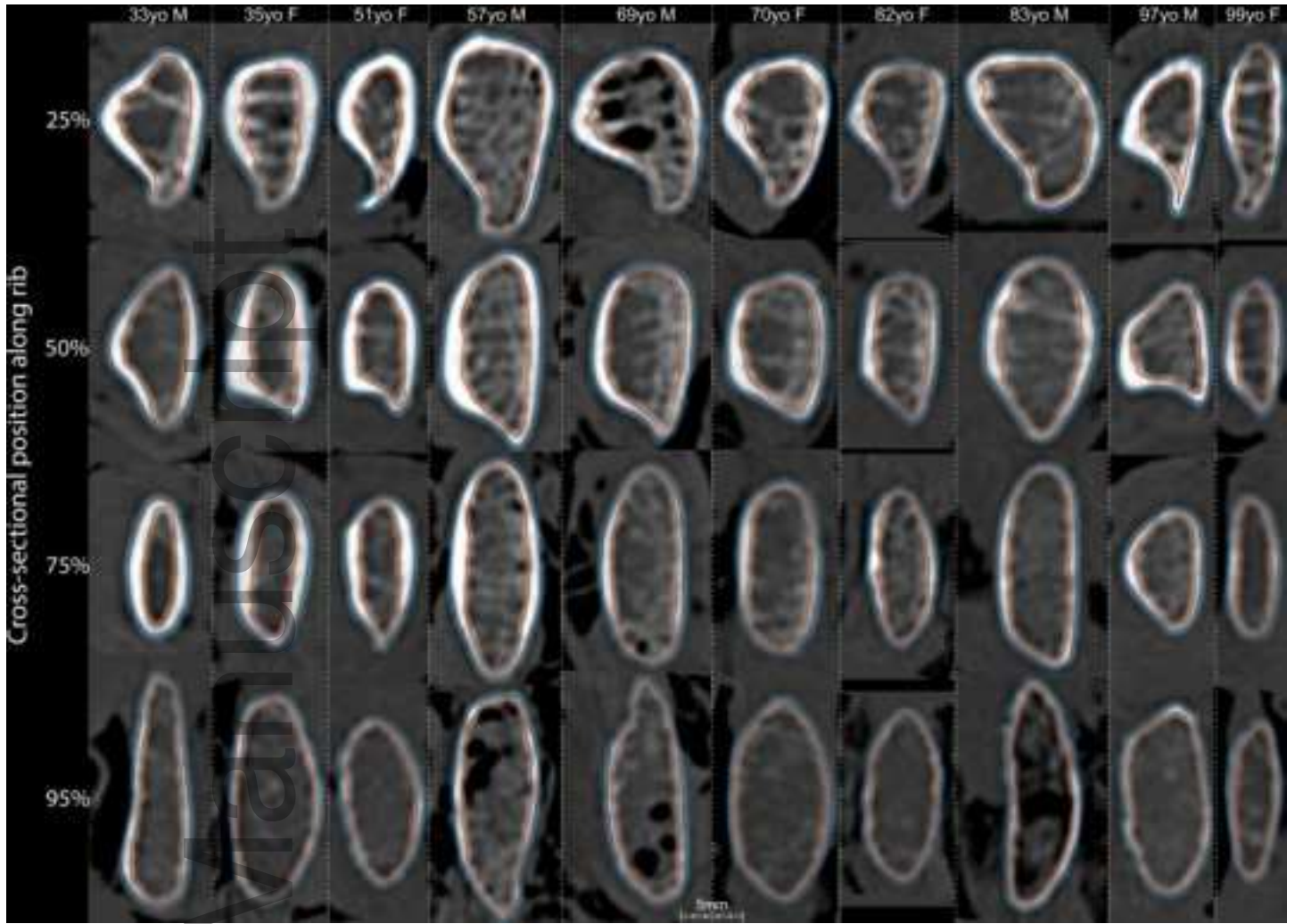teoporosis*, *2011*, 1–6. URL: `http://dx.doi.org/10.4061/2011/457591`.
doi:`10.4061/2011/457591`.

29

joa_13045_f1.pdf

Overlay

CT section

Histology

Endosteal border
·············· Periosteal border

joa_13045_f2.png

sternal end

around rib (80)

along rib (301)

vertebral end

joa_13045_f3.tif

joa_13045_f4.pdf

Section position (% rib length)

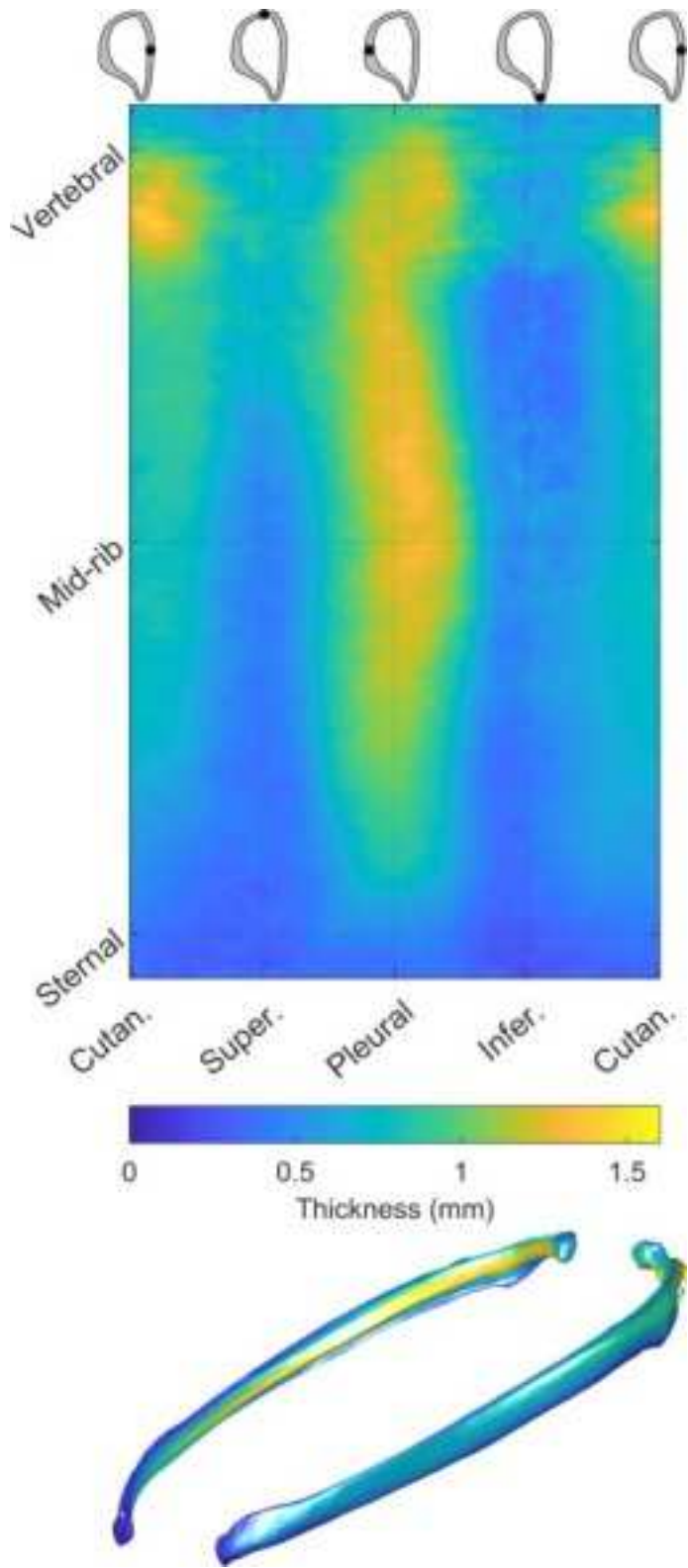Vertebral End   Sternal End

joa_13045_f6.png

joa_13045_f7.png